LiDAR-Aided Cooperative Localization and Environmental Perception for CAVs

Akif Adas, Luca Barbieri, Satyesh Awasthi, Pietro Morri, Simone Mentasti,
Stefano Arrigoni, Edoardo Sabbioni, Monica Nicoli
Politecnico di Milano, Milan, Italy

***Abstract*—This paper explores the potentialities of deploying vehicular Cooperative Positioning (CP) systems in urban scenarios utilizing real-world data collected via experimental campaigns. We examine the case of two prototype vehicles equipped with LiDAR sensors for perceiving their surrounding environment and with Global Navigation Satellite System (GNSS) receivers for positioning. The considered use case focuses on the cooperative detection of static landmarks, to be used for improving the vehicles' GNSS positioning. The experimental campaign points out a severe degradation in ego vehicle localization performances due to complex multipath propagation experienced in the urban scenario. To cope with such a problem, we integrate into the CP system a compensation method able to mitigate the position bias originating from the adverse propagating conditions. Experimental results show that integrating the developed compensation into the CP solution enables an accurate detection of the landmark positions, leading to an enhancement of the vehicle localization accuracy.**

***Index Terms*—Connected Automated Vehicles, Cooperative Positioning, LiDAR sensing, Global Navigation Satellite Systems**

I. Introduction

The emergence of Connected Automated Vehicles (CAVs) heralds a new era characterized by unprecedented levels of intelligence, sustainability, and safety [1]–[4]. One essential key for the rollout of CAVs is the requirement of accurate vehicular positioning to ensure dynamic environment adaptability [5]–[11]. Global Navigation Satellite System (GNSS) provides precise positioning, navigation, and timing information worldwide by exploiting a network of satellites in orbit around the Earth. GNSS Single Point Positioning (SPP) [12], [13] determines the position of a single receiver using satellite signals without any correction, while Satellite Based Augmentation Systems (SBAS) [14], [15] enhance positioning accuracy by providing additional correction signals to GNSS signals. Even though these currently represent the most commonly adopted solutions for positioning, their employment in dense urban environments is hindered by adverse satellite visibility and by multipath propagation conditions [16]–[18]. To augment positioning, some supplementary sensors have been incorporated, such as Inertial Measurement Unit (IMU), speedometer or steering angle, and sophisticated GNSS/Inertial Navigation System (GNSS/INS) solutions have been explored over time [19]–[23]. An alternative solution that complements GNSS is represented by Cooperative Positioning (CP) systems which improve the localization accuracy thanks to the coherent fusion of imaging and positioning measurements collected by multiple networked vehicles [24]–[27].

Recently, LiDAR-based CP approaches [28]–[36] have been gaining popularity thanks to the increasing penetration of LiDAR sensors on the vehicular market and their outstanding environmental sensing capabilities. In [28], the authors propose a decentralized data fusion approach that merges GNSS, LiDAR, and HD maps for improving the positioning performances, while [29] develops a cooperative Simultaneous Localization and Mapping (SLAM) approach for enhancing vehicle pose estimation. Cooperative mapping approaches are studied in [30], [31] where local LiDAR maps gathered from multiple vehicles are combined in a unified manner, while Machine Learning (ML)-based cooperative sensing techniques are explored in [32]–[34]. Finally, the works in [35], [36] investigate data association approaches for cooperative perception based on LiDAR sensors. Implementing CP methods based on LiDAR in real-world scenarios presents notable challenges. The foremost obstacle arises from multipath interference in urban environments, leading to signal degradation and compromised GNSS localization performance. A secondary challenge stems from the intricacies involved in processing point clouds across diverse LiDAR resolutions and attaining precise calibration for a range of onboard sensors.

This paper explores the potentialities of deploying LiDAR-based Implicit Cooperative Positioning (ICP) systems in real-world urban scenarios. ICP introduced in [37]–[40], which exploits the detections made by multiple vehicles about possible landmarks present in their surroundings to improve positioning accuracy without exchanging raw images/point clouds with other road units, e.g., Road Side Unit (RSU) or vehicle. Thereby, the privacy of road users is maintained, and the need for a low data rate is fulfilled. To highlight the challenges associated with deploying ICP using real-world data, we conducted several experimental campaigns with two prototype vehicles: each equipped with a LiDAR sensor and two GNSS units (one based on SPP exploiting SBAS, when available, and one integrating Real-Time Kinematics (RTK) corrections used as ground-truth) in an area reproducing common urban characteristics, comprising a large green area with trees at one end and buildings at the other. This geometric configuration influences satellite visibility therefore, the position accuracy provided by the SPP-based GNSS system varies widely ac-

This work is financed by the European Union—NextGenerationEU (National Sustainable Mobility Center CN00000023, Italian Ministry of University and Research Decree n. 1033—17/06/2022, Spoke 9)

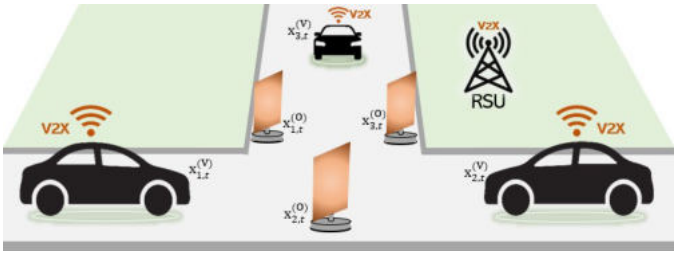

Fig. 1. Vehicular ICP scenario with the connected vehicles and three jointly sensed (passive) anchor points.

cording to whether SBAS is used or not. The data collected via the experimental campaign shows that severe positioning accuracy degradation is experienced in the urban scenario due to Non-Line of Sight (NLOS) propagation experienced by the GNSS receivers, making SPP inaccurate and also ICP partially less effective. To overcome this challenge, we propose compensating for the NLOS bias via a Bayesian tracking filter that jointly tracks the vehicles' position and the NLOS bias over time. Experimental results show that the developed Bayesian filtering solution substantially enhances the positioning estimate provided by the SPP-based GNSS unit. Besides, its integration into the ICP framework is shown to be beneficial for reducing vehicle positioning uncertainty.

The remainder of this paper is organized as follows. Sec. II introduces the system model for the considered CP positioning approach. Sec. III details the overall CP method outlining the object detection, the Bayesian filtering solution with bias compensation, and the cooperative fusion scheme. Sec. IV details the experimental campaign and provides the localization performance assessment. Finally, Sec. V draws conclusions.

II. System model

According to the ICP framework, we consider the vehicular scenario depicted in Fig. 1 where a set $\mathcal{V} = \{1, \dots, N_{\mathrm{V}}\}$ of N_{V} vehicles move in a 2D area. Each vehicle v, with $v \in \mathcal{V}$, is compactly described by its state $\mathbf{x}_{v,t}^{(\mathrm{V})} = [\mathbf{u}_{v,t}^{(\mathrm{V})}, \mathbf{v}_{v,t}^{(\mathrm{V})}]^{\mathrm{T}}$ where $\mathbf{u}_{v,t}^{(\mathrm{V})}$ and $\mathbf{v}_{v,t}^{(\mathrm{V})}$ are the 2D position and 2D velocity, respectively. We assume that the vehicle state evolves over time following a nearly constant velocity motion model defined as

$$\mathbf{x}_{v,t}^{(\mathrm{V})} = \mathbf{F}\mathbf{x}_{v,t-1}^{(\mathrm{V})} + \mathbf{L}\mathbf{q}_{v,t-1}^{(\mathrm{V})}, \tag{1}$$

where $\mathbf{F} = [\mathbf{I}_2\, T_s\mathbf{I}_2\,; \mathbf{0}_{2\times 2}\, \mathbf{I}_2]$ and $\mathbf{L} = [0.5T_s^2\mathbf{I}_2\,; T_s\mathbf{I}_2]$, T_s the sampling interval, while $\mathbf{q}_{v,t-1}^{(\mathrm{V})} \sim \mathcal{N}(\mathbf{0}, \mathbf{I}_2\sigma_{v,\mathrm{U}}^2)$ is a zero-mean Gaussian random variable with standard deviation $\sigma_{v,\mathrm{U}}$ modeling the acceleration uncertainty of the v-th vehicle. While moving in the driving environment, vehicles are able to detect objects via a dedicated object detection method (see Sec. III-A), termed as Grid-based Spatial Detector (GSD). These detections are then used by ICP for positioning refinement. The set of detectable (static) objects all over the scenario is denoted as $\mathcal{O} = \{1, \dots, N_{\mathrm{O}}\}$ with cardinality N_{O}. Each object $o \in \mathcal{O}$ has an associated state $\mathbf{x}_{o,t}^{(\mathrm{O})} = \mathbf{u}_{o,t}^{(\mathrm{O})}$ which is described only by the 2D position. The position evolution of each object state follows a static motion model, namely $\mathbf{x}_{o,t}^{(\mathrm{O})} = \mathbf{x}_{o,t-1}^{(\mathrm{O})}$, as only fixed objects are considered.

As far as the localization measurements are concerned, each vehicle $v \in \mathcal{V}$ is equipped with a GNSS unit whose output is

$$\boldsymbol{\rho}_{v,t}^{(\mathrm{V})} = \mathbf{T}\mathbf{x}_{v,t}^{(\mathrm{V})} + \mathbf{n}_{v,t}^{(\mathrm{V})}, \tag{2}$$

where $\mathbf{T} = [\mathbf{I}_2, \mathbf{0}_{2\times 2}]$, while $\mathbf{n}_{v,t}^{(\mathrm{V})} \sim \mathcal{N}(\mathbf{0}, \mathbf{I}_2\sigma_{v,\mathrm{P}}^2)$ is a zero-mean Gaussian random variable with standard deviation $\sigma_{v,\mathrm{P}}^2$ characterizing the GNSS position accuracy of the v-th vehicle. Instead, the detected objects vary over time according to the LiDAR sensing range R_s and their visibility. Specifically, at time t, the set of detected objects at vehicle v is $\mathcal{O}_{v,t} = \{k \in \mathcal{O} : \|\mathbf{u}_{v,t}^{(\mathrm{V})} - \mathbf{x}_{o,t}^{(\mathrm{O})}\| \leq R_s\} \subseteq \mathcal{O}$. This set is obtained by applying GSD over the point cloud $\mathbf{P}_{v,t} = [\mathbf{p}_{v,1,t}, \dots, \mathbf{p}_{v,N_\ell,t}]^{\mathrm{T}}$ of N_ℓ points collected by vehicle v at time t. GSD provides at the output a set of measurements $\boldsymbol{\rho}_{v,t}^{(\mathrm{L})} = \{\boldsymbol{\rho}_{v,o,t}^{(\mathrm{L})}\}_{o=1}^{|\mathcal{O}_{v,t}|}$ that refer to the 2D position of the detected objects (in the LiDAR frame of reference) and are defined as

$$\boldsymbol{\rho}_{v,o,t}^{(\mathrm{L})} = \mathbf{x}_{o,t}^{(\mathrm{L})} + \mathbf{n}_{v,o,t}^{(\mathrm{L})}, \tag{3}$$

where $n_{v,o,t}^{(\mathrm{L})} \sim \mathcal{N}(0, \mathbf{I}_2\sigma_{\mathrm{L}}^2)$ is a Gaussian random variable with standard deviation σ_{L} accounting for the combined error originating from GSD and the point cloud. For positioning refinement, the GSD measurements are converted from the local LiDAR frame to a global one. To do so, each element in the measurement set $\boldsymbol{\rho}_{v,t}^{(\mathrm{L})}$ is projected as follows

$$\boldsymbol{\rho}_{v,o,t}^{(\mathrm{G})} = \mathbf{R}_{v,t}\tilde{\boldsymbol{\rho}}_{v,o,t}^{(\mathrm{L})} = \mathbf{x}_{v,o,t}^{(\mathrm{G})} + \mathbf{n}_{v,o,t}^{(\mathrm{G})} \tag{4}$$

where $\tilde{\boldsymbol{\rho}}_{v,o,t}^{(\mathrm{L})} = [\boldsymbol{\rho}_{v,o,t}^{(\mathrm{L})^{\mathrm{T}}}, 1]^{\mathrm{T}}$, $\mathbf{x}_{v,o,t}^{(\mathrm{G})}$ is the object position in global reference frame and $\mathbf{n}_{v,o,t}^{(\mathrm{G})} \sim \mathcal{N}(\mathbf{0}, \sigma_L^2\mathbf{R}_{v,t}\mathbf{R}_{v,t}^{\mathrm{T}})$ is the noise with

$$\mathbf{R}_{v,t} = \begin{bmatrix} \cos(\alpha_{v,t}) & -\sin(\alpha_{v,t}) & t_{v,x} \\ \sin(\alpha_{v,t}) & \cos(\alpha_{v,t}) & t_{v,y} \\ 0 & 0 & 1 \end{bmatrix} \tag{5}$$

where $t_{v,x}$ and $t_{v,y}$ are the displacement between the LiDAR and GNSS unit over the x and y axis at the v-th vehicle while $\alpha_{v,t}$ the yaw angle. The yaw angle is estimated for each vehicle $v \in \mathcal{V}$ starting from the velocity provided by the motion model in (1) as

$$\alpha_{v,t} = \tan^{-1}(\mathbf{v}_{v,t,x}^{(\mathrm{V})}/\mathbf{v}_{v,t,y}^{(\mathrm{V})}) \tag{6}$$

and then smoothed out employing a moving median filter. Note that more advanced strategies could be used to get a better estimation of the yaw angle by incorporating IMUs in the vehicular setup [41], [42]. After the projection stage, the set of available measurements at vehicle v is $\boldsymbol{\rho}_{v,t}^{(\mathrm{O})} = \{\boldsymbol{\rho}_{v,o,t}^{(\mathrm{O})}\}_{o=1}^{|\mathcal{O}_{v,t}|}$ where each element is

$$\boldsymbol{\rho}_{v,o,t}^{(\mathrm{O})} = \boldsymbol{\rho}_{v,o,t}^{(\mathrm{G})} - \mathbf{u}_{v,t}^{(\mathrm{V})} = \mathbf{x}_{v,o,t}^{(\mathrm{G})} - \mathbf{u}_{v,t}^{(\mathrm{V})} + \mathbf{n}_{v,o,t}^{(\mathrm{G})} \tag{7}$$

which is used by ICP to refine the vehicle positioning. It is important to highlight that detected objects on LiDAR point cloud must be projected based on the mounting positions of LiDAR and GNSS antenna.

III. Cooperative positioning approach

This section briefly reviews the overall ICP paradigm extended to counteract GNSS measurements affected by multipath propagation. Specifically, in Sec. III-A, we introduce the developed object detector, namely GSD. Then, we describe in Sec. III-B the proposed bias compensation method and its integration into ICP (Sec. III-C).

A. Grid-based 3d object detection

Unlike conventional ML-based detectors, GSD aims at extracting the positions of the objects via suitable processing of the LiDAR point clouds without requiring any labeled data. By doing so, we aim to provide an effective detector that is potentially applicable to any driving environment and does not suffer from large performance drops when the scenario or the spatial resolution of the LiDAR sensors is changed. This is a common problem encountered in ML-based 3D object detectors that it is still an active area of research [43]–[46]. In what follows, we break down the main operations performed by GSD and describe how the bounding boxes are generated.

The goal is to detect any commonly detectable anchor point, including compact road elements, e.g., road cones, tree trunks, pedestrians, trash bins, and poles. To do so, GSD seeks to recognize isolated point clusters by leveraging changes in point density within the scene. The block diagram of GSD is shown in fig. 2. The process begins by embedding a reference (anchor) point cluster, which is a spherical sparse point cloud, at a dynamically chosen known location in order to reduce the error, i.e., segmentation into grids, introduced in the following steps. It is followed by the elimination of redundant points that are outside of the desired area. This area should be chosen according to road-sideway arrangement that varies between cities. If there is no preference for observation, this step can be skipped for the cost of increasing computational burden. After filtering the redundant points, the ground layer is removed, and outlier elimination is performed as in [47]. This filtering is significant for lightening the rest of the process. The next process is to project the filtered point cloud onto the xy plane and create a 2D density map. This transformation is a vector operation and is a candidate to be the bottleneck for high-density point clouds. A density map allows the programmer to observe the scene while taking advantage of the required domain expertise and further eliminate rambling points by filtering according to the density of each segment. The heart of GSD is a density-based clustering method referred to as Density-Based Spatial Clustering of Applications with Noise (DBSCAN) [48]. The algorithm groups nearby data points into clusters, designating certain points as idle if they fail to meet the criteria for cluster membership. GSD assumes that objects are well separated from each other and other entities. Considering this assumption, large clusters, such as walls, buses, and cars are neglected. The remaining clusters are considered road elements, and their 2D locations are calculated by averaging on the 2D voxel map. Finally, the embedded point cluster is exploited to eliminate processing errors. This operation has been repeated by finding the minimum distance between the closest detected object and the reference cluster. Occasionally, the filtering processes have removed the anchor cluster, which results in the failure of the optimization phase, which is the process of compensation for the shift that happens during segmentation. To overcome this issue, the anchor cluster shifts randomly to another location until either the optimization procedure completes properly or the repetition number reaches five.

B. Bayesian filtering with multipath compensation

Under urban scenarios, GNSS signals might be shadowed or completely blocked due to poor satellite visibility giving rise to ranging bias due to multipath. To overcome this problem, we propose to employ a Bayesian filtering approach to compensate for the bias. Specifically, we extend the model introduced in (1) to account for possible position biases present in the GNSS measurements. The new model is

$$\mathbf{s}_{v,t}^{(\mathrm{V})} = \mathbf{K}\mathbf{s}_{v,t-1}^{(\mathrm{V})} + \mathbf{P}\mathbf{w}_{v,t-1}^{(\mathrm{V})} \tag{8}$$

where $\mathbf{s}_{v,t}^{(\mathrm{V})} = [\mathbf{x}_{v,t}^{(\mathrm{V})^{\mathrm{T}}}, \mathbf{b}_{v,t}^{(\mathrm{V})}]^{\mathrm{T}}$ where $\mathbf{b}_{v,t}^{(\mathrm{V})}$ is an additional state that contains the bias caused by NLOS propagation over the x and y axis, while $\mathbf{w}_{v,t-1}^{(\mathrm{V})} \sim \mathcal{N}(\mathbf{0}, \mathbf{W})$ where $\mathbf{W} = \mathrm{blkdiag}(\sigma_{v,\mathrm{U}}^2\mathbf{I}_2, \sigma_{v,\mathrm{B}}^2\mathbf{I}_2)$ with $\sigma_{v,\mathrm{B}}$ being the standard deviation modeling the uncertainty on the GNSS bias. Matrices in (8) are defined as $\mathbf{K} = [\mathbf{F}\mathbf{0}_{4\times2}; \mathbf{0}_{2\times4}\mathbf{I}_2]$ and $\mathbf{P} = [\mathbf{L}\mathbf{0}_{4\times2}; \mathbf{0}_{2\times2}\mathbf{I}_2]$. Besides introducing an explicit bias formulation in the state evolution, we modify the modeling related to the GNSS measurements to account for possible NLOS impairments. Accordingly, we have

$$\boldsymbol{\rho}_{v,t}^{(\mathrm{V})} = \mathbf{B}\mathbf{s}_{v,t}^{(\mathrm{V})} + \mathbf{n}_{v,t}^{(\mathrm{V})} \tag{9}$$

where $\mathbf{B} = [\mathbf{I}_2\mathbf{0}_{2\times2}\mathbf{I}_2]$ while $\mathbf{n}_{v,t}^{(\mathrm{V})}$ is the same noise defined in (2). All the other modeling detailed in Sec. II to extract the object location measurements remain unchanged. To estimate the state $\mathbf{s}_{v,t}^{(\mathrm{V})}$ over time, we resort to a Bayesian tracking algorithm. Considering that all models are linear and the noise distributions Gaussian, the state can be estimated using a Kalman Filter (KF) whose solution is

$$\hat{\mathbf{s}}_{v,t}^{(\mathrm{V})} = \hat{\mathbf{s}}_{v,t|t-1}^{(\mathrm{V})} + \mathbf{G}_t\left(\boldsymbol{\rho}_{v,t}^{(\mathrm{V})} - \mathbf{B}\hat{\mathbf{s}}_{v,t|t-1}^{(\mathrm{V})}\right) \tag{10}$$

$$\mathbf{C}_t^{(\mathrm{KF})} = \mathbf{C}_{t|t-1}^{(\mathrm{KF})} - \mathbf{G}_t\mathbf{B}\mathbf{C}_{t|t-1}^{(\mathrm{KF})} \tag{11}$$

where $\mathbf{G}_t = \mathbf{C}_{t|t-1}^{(\mathrm{KF})}\mathbf{B}^{\mathrm{T}}\left(\mathbf{B}\mathbf{C}_{t|t-1}^{(\mathrm{KF})}\mathbf{B}^{\mathrm{T}} + \sigma_{v,\mathrm{P}}^2\mathbf{I}_2\right)^{-1}$ is the Kalman gain while $\hat{\mathbf{s}}_{v,t|t-1}^{(\mathrm{V})}$ is obtained by applying the motion model in (8) over the previous estimated state $\hat{\mathbf{s}}_{t-1|t-1}^{(\mathrm{V})}$.

C. Cooperative positioning solution

After compensating for the NLOS effects experienced by the GNSS, the ICP takes as input the bias-compensated measurements and enhances the positioning performances thanks to the coherent combination of multiple measurements gathered across interconnected vehicles.

Let $\boldsymbol{\theta}_t = [\mathbf{x}_t^{(\mathrm{V})^{\mathrm{T}}}\mathbf{x}_t^{(\mathrm{O})^{\mathrm{T}}}]^{\mathrm{T}}$ represent the fused state merging all the vehicles $\boldsymbol{x}_t^{(\mathrm{V})} = [\mathbf{x}_{v,t}^{(\mathrm{V})}]_{v\in\mathcal{V}}$ and all objects $\mathbf{x}_t^{(\mathrm{O})} = [\mathbf{x}_{o,t}]_{o\in\mathcal{O}}$

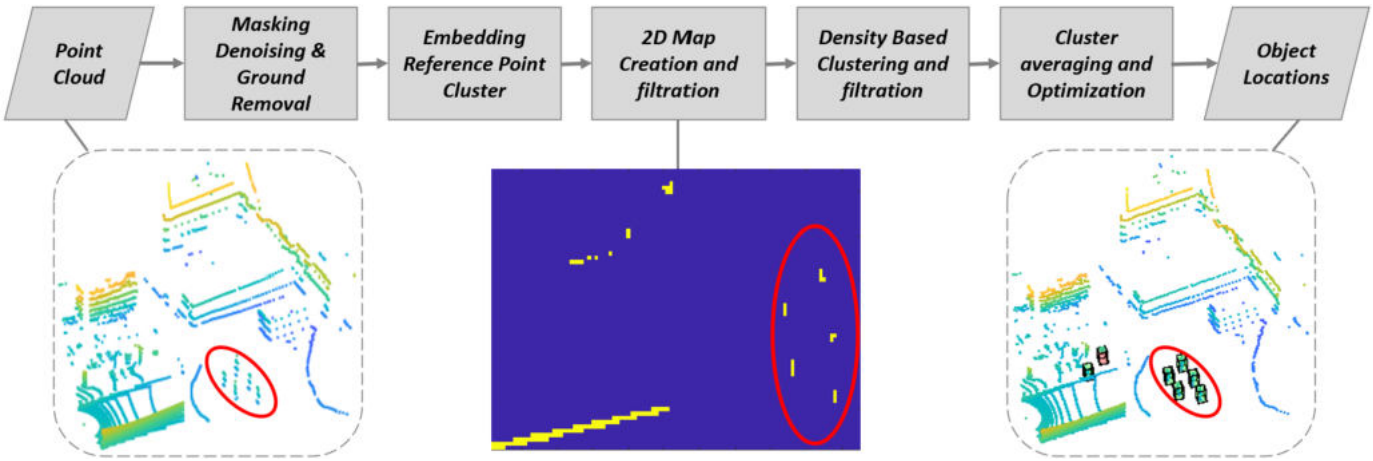

Fig. 2. GSD network overview.

states. Similarly, we define the overall set of measurements as $\boldsymbol{\rho}_t = [\tilde{\boldsymbol{\rho}}_t^{(\mathrm{V})^{\mathrm{T}}} \boldsymbol{\rho}_t^{(\mathrm{O})^{\mathrm{T}}}]^{\mathrm{T}}$ where $\tilde{\boldsymbol{\rho}}_t^{(\mathrm{V})} = [\tilde{\boldsymbol{\rho}}_{v,t}^{(\mathrm{V})}]_{v\in\mathcal{V}}$ collects the corrected GNSS measurements from all vehicles which are evaluated as

$$\tilde{\boldsymbol{\rho}}_{v,t}^{(\mathrm{V})} = \boldsymbol{\rho}_{v,t}^{(\mathrm{V})} - \widehat{\mathbf{b}}_{v,t}^{(\mathrm{V})} \tag{12}$$

where $\widehat{\mathbf{b}}_{v,t}^{(\mathrm{V})}$ is obtained from the state estimates provided in (10). On the other hand, $\boldsymbol{\rho}_t^{(\mathrm{O})} = [\boldsymbol{\rho}_{v,o,t}^{(\mathrm{O})}]_{v\in\mathcal{V},o\in\mathcal{O}_{v,t}}$ aggregates the measurements about the detected objects. The overall set of measurements can be explicitly written as

$$\boldsymbol{\rho}_t = \mathbf{H}_t\boldsymbol{\theta}_t + \mathbf{n}_t, \tag{13}$$

where $\mathbf{H}_t$ is computed as in [37], while $\mathbf{n}_t = [\mathbf{n}_t^{(\mathrm{V})^{\mathrm{T}}} \mathbf{n}_t^{(\mathrm{O})^{\mathrm{T}}}]^T$ with $\mathbf{n}_t^{(\mathrm{V})} = [\mathbf{n}_{v,t}^{(\mathrm{V})}]_{v\in\mathcal{V}}$ and $\mathbf{n}_{v,t}^{(\mathrm{O})} = [\mathbf{n}_{v,o,t}^{(\mathrm{G})}]_{o\in\mathcal{O}}$. The noise is $\mathbf{n}_t \sim \mathcal{N}(\mathbf{0}, \boldsymbol{\Sigma}_t)$ where $\boldsymbol{\Sigma}_t = \mathrm{blkdiag}(\sigma_{1,\mathrm{P}}^2\mathbf{I}_2, \ldots, \sigma_{N_{\mathrm{V}},\mathrm{P}}^2\mathbf{I}_2, \sigma_{\mathrm{L}}^2\mathbf{R}_{v,t}\mathbf{R}_{v,t}^{\mathrm{T}} \otimes \mathbf{I}_{N_{\mathrm{O}}})$. To estimate the overall state, we resort to the Minumum Mean Square Error (MMSE) criterion which reduces to a cooperative KF as all the noise statistics are Gaussian and the models linear. Formaly, the MMSE estimate is given by [37]

$$\widehat{\boldsymbol{\theta}}_{t|t} = \widehat{\boldsymbol{\theta}}_{t|t-1} + \mathbf{C}_{t|t}^{(\mathrm{ICP})}\mathbf{H}_t^{\mathrm{T}}\boldsymbol{\Sigma}_t^{-1}\left(\boldsymbol{\rho}_t - \mathbf{H}_t\widehat{\boldsymbol{\theta}}_{t|t-1}\right), \tag{14}$$

where $\hat{\boldsymbol{\theta}}_{t|t-1}$ is obtained by propagating $\hat{\boldsymbol{\theta}}_{t-1|t-1}$ according to the motion models presented in Sec. II while the covariance $\mathbf{C}_{t|t}^{(\mathrm{ICP})}$ is evaluated as in [37].

IV. Experimental Results

This section assesses the developed method in a real-world scenario. In Sec. IV-A we describe the vehicles' setup and the data collection process adopted. Then, Sec. IV-B and Sec. IV-C present the results characterizing the performances of the object detection step and the overall ICP algorithm.

A. Vehicle Setup and Urban Area

The scenario considered in this work consists of two prototype vehicles traveling toward each other in different lanes and approaching a crosswalk where the test obstacles remain stationary. Vehicles are shown in fig. 3. The first vehicle (Veh1), is a small full electric bus commercially used as a first and last-mile solution or a shuttle in airports and universities; the one owned by our research group has a custom setup, elaborated in [49], for scientific research. The other vehicle (Veh2) is a quadricycle vehicle specifically instrumented by our research group. Its main mechanical and electrical characteristics are reported in [50] along with its sensor setup. Each vehicle is equipped with two independent GNSS units developed by Swift Navigation. One of these GNSS units is augmented by RTK correction via Internet Protocol (IP) to keep a record of the Ground Truth (GT) positions of the vehicles. GPS-702-GG and GPS500 antennas serve the RTK-corrected GNSS units on Veh1 and Veh2, respectively. The remaining GNSS units gather data for enhancement through the proposed method, receiving GNSS and SBAS messages via mini survey receiver antenna GPS500 and MIKE3A antennas on Veh1 and Veh2.

The GPS-702-GG and GPS500 antennas have low antenna gain. Here, the drop in signal level is compensated by a high-gain Low Noise Amplifier (LNA). The other antenna, Siretta MIKE3A, is relatively cheaper and more accessible with a higher antenna gain. This difference between the two antennas has a direct impact on satellite visibility and causes SBAS services for the second vehicle to be unavailable for a period of time due to an obstructed sky condition.

The other sensing component used by the vehicles is the LiDAR sensor. The LiDAR sensor deployed on Veh1 is a Velodyne Puck (VLP-16) [51] that has 16 channels and $125K$ points per second point cloud density. On the other hand, Veh2 has Hesai Pandar XT32 with 32 channels and $250K$ points per second point cloud density [52]. It is important to highlight that detected objects on LiDAR point cloud must be projected based on the mounting positions of LiDAR and GNSS antenna. Table.I summarises vehicles' instrumental setups.

B. Data Acquisition and Interim Outcomes

The measurements are recorded locally in each vehicle through Robot Operation System (ROS). This data is then transferred to a computing unit. This artificially realizes the situation where vehicles are connected to the central compu-

Fig. 3. Prototype vehicles with Veh1 on the left and Veh2 on the right.

TABLE I
VEHICLE INSTRUMENTATION

Veh.	LiDAR		GNSS		
	Model	Planes	Model	Antenna	RTK
1	Velodyne Puck	16	SwiftNav Piksi	GPS500	×
			Swiftnav Piksi	GPS-702-GG	✓
2	Hesai PandarXT32	32	SwiftNav Duro	MIKE3A	×
			Swiftnav Piksi	GPS500	✓

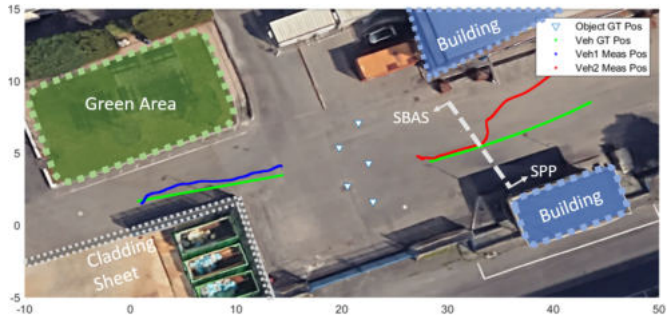

Fig. 4. Measured vehicle trajectories display GNSS measurements alongside RTK-corrected GT poses. Specific zones within the region have been delineated, indicating the utilization of SBAS and SPP solutions in two zones.

tational unit. The data used in this paper was obtained from a 4-minute data acquisition session based on the aforementioned scenario. When measurements are collected centrally, some synchronization errors occur due to the different recording speeds of the used sensors. The sensor outputs are synchronized by considering the clock information transmitted by the internet-based GNSS RTK correction method. All collected data was reduced to 10Hz and thus a common recording frequency was achieved.

Throughout these experiments, efforts were directed toward enhancing the optimal single-receiver GNSS position solution. When accessible, ego-vehicle positioning is determined taking into account the SBAS-derived positions; otherwise, the SPP position fix is employed. The availability of SBAS in the considered area is 100% for Veh1 and 36% for Veh2 and the corresponding single-receiver GNSS position Root Mean Square Error (RMSE) values are 0.61 m and 2.04 m, respectively. Considering the combination of SBAS and SPP measurements, the most likely scenario to be encountered

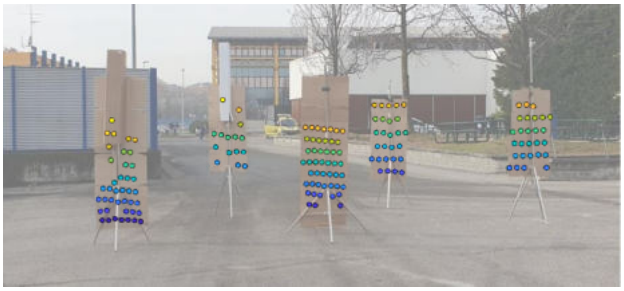

Fig. 5. The projected point cloud of test objects onto camera imagery.

TABLE II
THE IMPACT OF THE POSITIONING SOLUTION ON OBJECT DETECTION AND ASSOCIATION.

Position	TP Det. Rate [%]		OD RMSE [m]	
	Veh1	Veh2	Veh1	Veh2
RTK-Corrected	99.61	99.23	0.38	0.24
NLOS-Compensation	98.15	78.47	0.56	1.08
GNSS-Raw	92.8	60.82	0.92	2.52

in real life has been obtained. A portion of the vehicle trajectories is shown in fig. 4 where the green line represents the GT location fix, while the blue and red ones are the ego-GNSS measurements for Veh1 and Veh2, respectively, and the triangles represent GT object locations.

Concurrently, LiDAR sensors are actively generating point clouds. These point clouds are fed to the object detector proposed in Sec. III-A, and the object positions are obtained. These positions are defined in the LiDAR coordinate system. Since they should be mapped in the same reference system, the LiDAR-GNSS calibration process given in Sec. II is applied. Upon analyzing the SPP solutions of the vehicles, it is noted that they exhibit a significant and fluctuating bias in comparison to the actual positions. Particularly, the signal quality of Veh2 experienced more deterioration. In order to overcome this problem, Bayesian filter-based bias estimation, given in Sec. II, is performed. This filter assumes that the observed bias is almost constant and it makes predictions based on a random walk model. The standard deviations associated with the random walk bias model were calibrated over a non-exhaustive grid search. After the bias elimination, also referred to as NLOS compensation, vehicle position RMSE values were reduced to 0.37 m (39% enhancement) for Veh1 and 0.91 m (55% enhancement) for Veh2 with respect to the single-receiver GNSS positions. This augmented location information is then used for LiDAR-GNSS calibration. As a result, the True Positive (TP) object detection rate, which is listed in Table. II, enhances with respect to the calibration with raw GNSS positioning. Likewise, this resulted in an improvement in the performance of ego object positioning within the global reference system.

Fig. 6 shows the Empirical Cumulative Density Function (ECDF) of the object detection error accumulated with LiDAR-GNSS calibration for the translation handled considering RTK-corrected, NLOS compensated and raw GNSS vehicle locations. Here, the impact of the positioning technique

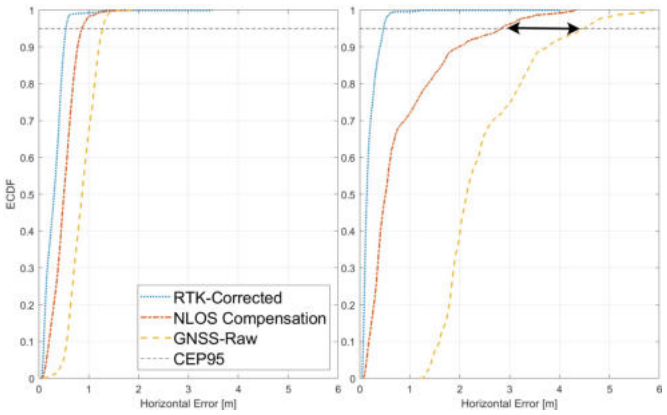

Fig. 6. ECDF of the average object positioning error for Veh1 on the left and Veh2 on the right.

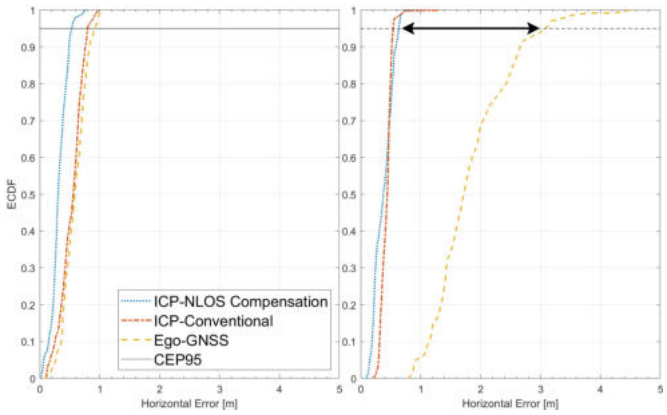

Fig. 7. ECDF of the positioning errors with CEP95 highlighted for Veh1 on the left and Veh2 on the right.

on object detection accuracy is investigated by comparing the following cases: (i) The positioning using RTK-corrected locations; (ii) the NLOS compensated positions; (iii) the GNSS position solutions. The Circular Error Probable with 95% confidence (CEP95) values are 0.53 m, 0.83 m and 1.26 m for the Veh1 and 0.46 m, 2.74 m, and 4.4 m for the Veh2, respectively. Thereby, the significance of having accurate vehicular positioning for detecting objects in the global reference system has been highlighted and more reliable late collaboration [53] members were obtained by NLOS compensation approach given in Sec.II.

C. Overall Results

After obtaining the global object locations and the ego vehicle locations, the CP integrates two vehicles' observations into a cooperative filter in the central computational unit. The achieved results with the proposed method are presented in fig. 7. Ego-GNSS pertains to self-positioning, ICP with NLOS compensation represents CP based on bias-compensated vehicles' locations, and ICP-GNSS corresponds to CP performed using the recorded GNSS position fixes. Findings indicate that ICP reduces localization error by 41% for Veh1 and 42% for Veh2 with respect to non-cooperative positioning, in terms of CEP95. When the outcomes of ICP are compared, these findings show that collaboration aids in mitigating multipath bias for the affected vehicle (Veh2) by utilizing the other vehicle as a reference or anchor for correction. This correction is based on the fact that the vehicle with better ego positioning also provides more accurate object recognition. Thus, the accuracy of the vehicles is augmented and consequently, non-cooperative road objects are included in the collaborative ecosystem.

V. Conclusions

In this paper, we explored the potential of the LiDAR-aided ICP in vehicular localization to provide highly accurate positioning by exploiting the presence of surrounding road objects. In particular, we developed a CP method for performing cooperative sensing, achieved by proposing a novel object detector, GSD, for sparse LiDAR point clouds, and cooperative positioning by developing a custom Kalman filter. The developed method has been validated by conducting several data acquisitions in a suburban area. These acquisitions have been designed to account for different single-receiver GNSS position fix abilities to leverage reality. Beyond the outcomes, some challenges of sensor calibration have been stressed. Finally, vehicular positioning has experienced an average augmentation of 41.5% across two test vehicles, and numerical results have indicated the superior performance of the proposed method when compared to a non-cooperative approach. In addition to this, the benefits of the cooperative solution on different sensors and data quality acquired by multiple vehicles have been demonstrated, such as the fact that the cooperation member, which is more influenced by the factors that degrade the position solution quality of GNSS, can benefit from this collaboration and avoid these effects.

Future works will target the inclusion of infrastructure in the system as an observer with a known location and high object recognition accuracy. Hence, the benefits of using an observer as an anchor point will be further investigated.

References

[1] M. Boban, A. Kousaridas, K. Manolakis *et al.*, "Connected roads of the future: Use cases, requirements, and design considerations for vehicle-to-everything communications," *IEEE Vehicular Technology Magazine*, vol. 13, no. 3, pp. 110–123, 2018.

[2] E. Yurtsever, J. Lambert, A. Carballo *et al.*, "A survey of autonomous driving: Common practices and emerging technologies," *IEEE Access*, vol. 8, pp. 58 443–58 469, 2020.

[3] A. Eskandarian, C. Wu, and C. Sun, "Research advances and challenges of autonomous and connected ground vehicles," *IEEE Transactions on Intelligent Transportation Systems*, vol. 22, no. 2, pp. 683–711, 2021.

[4] A. Matin and H. Dia, "Impacts of connected and automated vehicles on road safety and efficiency: A systematic literature review," *IEEE Transactions on Intelligent Transportation Systems*, vol. 24, no. 3, pp. 2705–2736, 2023.

[5] N. Alam and A. G. Dempster, "Cooperative positioning for vehicular networks: Facts and future," *IEEE Transactions on Intelligent Transportation Systems*, vol. 14, no. 4, pp. 1708–1717, 2013.

[6] S. Kuutti, S. Fallah, K. Katsaros *et al.*, "A survey of the state-of-the-art localization techniques and their potentials for autonomous vehicle applications," *IEEE Internet of Things Journal*, vol. 5, no. 2, pp. 829–846, 2018.

[7] D. Kumar and N. Muhammad, "A survey on localization for autonomous vehicles," *IEEE Access*, vol. 11, pp. 115 865–115 883, 2023.

[8] Y. Lu, H. Ma, E. Smart *et al.*, "Real-time performance-focused localization techniques for autonomous vehicle: A review," *IEEE Transactions on Intelligent Transportation Systems*, vol. 23, no. 7, pp. 6082–6100, 2022.

[9] A. Yoganandhan, S. Subhash, J. Hebinson Jothi *et al.*, "Fundamentals and development of self-driving cars," *Materials Today: Proceedings*, vol. 33, pp. 3303–3310, 2020.

[10] A. Abosekeen, U. Iqbal, A. Noureldin *et al.*, "A novel multi-level integrated navigation system for challenging GNSS environments," *IEEE Transactions on Intelligent Transportation Systems*, vol. 22, no. 8, pp. 4838–4852, 2021.

[11] M. Maaref and Z. M. Kassas, "Ground vehicle navigation in GNSS-challenged environments using signals of opportunity and a closed-loop map-matching approach," *IEEE Transactions on Intelligent Transportation Systems*, vol. 21, no. 7, pp. 2723–2738, 2020.

[12] D. Medina, H. Li, J. Vilà-Valls *et al.*, "On robust statistics for GNSS single point positioning," in *2019 IEEE Intelligent Transportation Systems Conference (ITSC)*, 2019, pp. 3281–3287.

[13] A. Grenier, E. S. Lohan, A. Ometov *et al.*, "A survey on low-power GNSS," *IEEE Communications Surveys & Tutorials*, vol. 25, no. 3, pp. 1482–1509, 2023.

[14] D. Egea-Roca, M. Arizabaleta-Diez, T. Pany *et al.*, "GNSS user technology: State-of-the-art and future trends," *IEEE Access*, vol. 10, pp. 39 939–39 968, 2022.

[15] P. Zabalegui, G. De Miguel, A. Pérez *et al.*, "A review of the evolution of the integrity methods applied in GNSS," *IEEE Access*, vol. 8, pp. 45 813–45 824, 2020.

[16] E. D. Kaplan and C. J. Hegarty, *Understanding GPS/GNSS: principles and applications*. Artech house, 2017.

[17] J. Breßler, P. Reisdorf, M. Obst *et al.*, "GNSS positioning in non-line-of-sight context—a survey," in *2016 IEEE 19th International Conference on Intelligent Transportation Systems (ITSC)*, 2016, pp. 1147–1154.

[18] N. Zhu, J. Marais, D. Bétaille *et al.*, "GNSS position integrity in urban environments: A review of literature," *IEEE Transactions on Intelligent Transportation Systems*, vol. 19, no. 9, pp. 2762–2778, 2018.

[19] T.-S. Lou, N.-H. Chen, Z.-W. Chen *et al.*, "Robust partially strong tracking extended consider kalman filtering for INS/GNSS integrated navigation," *IEEE Access*, vol. 7, pp. 151 230–151 238, 2019.

[20] S. Lu, Y. Guo, H. Shang *et al.*, "Spoofing control strategy for precise position offset based on INS/GNSS tightly coupled navigation," *IEEE Access*, vol. 8, pp. 103 585–103 600, 2020.

[21] W. Wen, X. Bai, G. Zhang *et al.*, "Multi-agent collaborative GNSS/camera/INS integration aided by inter-ranging for vehicular navigation in urban areas," *IEEE Access*, vol. 8, pp. 124 323–124 338, 2020.

[22] X. Zhang, Z. Cheng, J. Ma *et al.*, "Semi-definite relaxation-based admm for cooperative planning and control of connected autonomous vehicles," *IEEE Transactions on Intelligent Transportation Systems*, vol. 23, no. 7, pp. 9240–9251, 2022.

[23] Y. Zhang, L. Wang, X. Jiang *et al.*, "An efficient LiDAR-based localization method for self-driving cars in dynamic environments," *Robotica*, vol. 40, no. 1, p. 38–55, 2022.

[24] M. Z. Win, A. Conti, S. Mazuelas *et al.*, "Network localization and navigation via cooperation," *IEEE Communications Magazine*, vol. 49, no. 5, pp. 56–62, 2011.

[25] N. Patwari, J. Ash, S. Kyperountas *et al.*, "Locating the nodes: cooperative localization in wireless sensor networks," *IEEE Signal Processing Magazine*, vol. 22, no. 4, pp. 54–69, 2005.

[26] H. Wymeersch, J. Lien, and M. Z. Win, "Cooperative localization in wireless networks," *Proceedings of the IEEE*, vol. 97, no. 2, pp. 427–450, 2009.

[27] N. Piperigkos, A. S. Lalos, and K. Berberidis, "Graph Laplacian diffusion localization of connected and automated vehicles," *IEEE Transactions on Intelligent Transportation Systems*, vol. 23, no. 8, pp. 12 176–12 190, 2022.

[28] E. Héry, P. Xu, and P. Bonnifait, "Consistent decentralized cooperative localization for autonomous vehicles using LiDAR, GNSS, and HD maps," *Journal of Field Robotics*, vol. 38, no. 4, pp. 552–571, 2021.

[29] S. Fang, H. Li, and M. Yang, "Lidar SLAM based multivehicle cooperative localization using iterated split CIF," *IEEE Transactions on Intelligent Transportation Systems*, vol. 23, no. 11, pp. 21 137–21 147, 2022.

[30] Y. Zhang, L. Chen, Z. XuanYuan *et al.*, "Three-dimensional cooperative mapping for connected and automated vehicles," *IEEE Transactions on Industrial Electronics*, vol. 67, no. 8, pp. 6649–6658, 2020.

[31] G. Luo, C. Shao, N. Cheng *et al.*, "EdgeCooper: Network-aware cooperative LiDAR perception for enhanced vehicular awareness," *IEEE Journal on Selected Areas in Communications*, vol. 42, no. 1, pp. 207–222, 2024.

[32] E. E. Marvasti, A. Raftari, A. E. Marvasti *et al.*, "Cooperative LIDAR object detection via feature sharing in deep networks," in *2020 IEEE 92nd Vehicular Technology Conference (VTC2020-Fall)*, 2020, pp. 1–7.

[33] ——, "Bandwidth-adaptive feature sharing for cooperative LIDAR object detection," in *2020 IEEE 3rd Connected and Automated Vehicles Symposium (CAVS)*, 2020, pp. 1–7.

[34] E. Arnold, M. Dianati, R. de Temple *et al.*, "Cooperative perception for 3D object detection in driving scenarios using infrastructure sensors," *IEEE Transactions on Intelligent Transportation Systems*, vol. 23, no. 3, pp. 1852–1864, 2022.

[35] B. Camajori Tedeschini, M. Brambilla, L. Barbieri *et al.*, "Cooperative lidar sensing for pedestrian detection: Data association based on message passing neural networks," *IEEE Transactions on Signal Processing*, vol. 71, pp. 3028–3042, 2023.

[36] ——, "Addressing data association by message passing over graph neural networks," in *2022 25th International Conference on Information Fusion (FUSION)*, 2022, pp. 01–07.

[37] G. Soatti, M. Nicoli, N. Garcia *et al.*, "Implicit cooperative positioning in vehicular networks," *IEEE Transactions on Intelligent Transportation Systems*, vol. 19, no. 12, pp. 3964–3980, 2018.

[38] M. Brambilla, M. Nicoli, G. Soatti *et al.*, "Augmenting vehicle localization by cooperative sensing of the driving environment: Insight on data association in urban traffic scenarios," *IEEE Transactions on Intelligent Transportation Systems*, vol. 21, no. 4, pp. 1646–1663, 2020.

[39] L. Barbieri, B. C. Tedeschini, M. Brambilla *et al.*, "Implicit vehicle positioning with cooperative lidar sensing," in *ICASSP 2023 - 2023 IEEE International Conference on Acoustics, Speech and Signal Processing (ICASSP)*, 2023, pp. 1–5.

[40] L. Barbieri, M. Brambilla, and M. Nicoli, "Deep neural networks for cooperative lidar localization in vehicular networks," in *ICC 2023 - IEEE International Conference on Communications*, 2023, pp. 185–190.

[41] H. Ahmed and M. Tahir, "Accurate attitude estimation of a moving land vehicle using low-cost MEMS IMU sensors," *IEEE Transactions on Intelligent Transportation Systems*, vol. 18, no. 7, pp. 1723–1739, 2017.

[42] Y. Wang, J. Mangnus, D. Kostić *et al.*, "Vehicle state estimation using GPS/IMU integration," in *SENSORS, 2011 IEEE*, 2011, pp. 1815–1818.

[43] J. Yang, S. Shi, Z. Wang *et al.*, "ST3D++: Denoised self-training for unsupervised domain adaptation on 3d object detection," *IEEE Transactions on Pattern Analysis and Machine Intelligence*, vol. 45, no. 5, pp. 6354–6371, 2023.

[44] Q. Xu, Y. Zhou, W. Wang *et al.*, "SPG: Unsupervised domain adaptation for 3D object detection via semantic point generation," in *2021 IEEE/CVF International Conference on Computer Vision (ICCV)*, 2021, pp. 15 426–15 436.

[45] Y. Wang, J. Yin, W. Li *et al.*, "SSDA3D: Semi-supervised domain adaptation for 3D object detection from point cloud," *Proceedings of the AAAI Conference on Artificial Intelligence*, vol. 37, no. 3, pp. 2707–2715, Jun. 2023.

[46] C. Saltori, S. Lathuilière, N. Sebe *et al.*, "SF-UDA3D: Source-free unsupervised domain adaptation for LiDAR-based 3D object detection," in *2020 International Conference on 3D Vision (3DV)*, 2020, pp. 771–780.

[47] R. B. Rusu, Z. C. Marton, N. Blodow *et al.*, "Towards 3D point cloud based object maps for household environments," *Robotics and Autonomous Systems*, vol. 56, no. 11, pp. 927–941, 2008.

[48] J. Shen, X. Hao, Z. Liang *et al.*, "Real-time superpixel segmentation by DBSCAN clustering algorithm," *IEEE Transactions on Image Processing*, vol. 25, no. 12, pp. 5933–5942, 2016.

[49] S. S. Awasthi, S. Arrigoni, P. Awasthi *et al.*, "An interactive human-machine control interface for an autonomous shuttle," in *2021 AEIT International Conference on Electrical and Electronic Technologies for Automotive (AEIT AUTOMOTIVE)*, 2021, pp. 1–6.

[50] S. Arrigoni, S. Mentasti, F. Cheli *et al.*, "Design of a prototypical platform for autonomous and connected vehicles," in *2021 AEIT International Conference on Electrical and Electronic Technologies for Automotive (AEIT AUTOMOTIVE)*, 2021, pp. 1–6.

[51] Velodyne, "Velodyne lidar puck datasheet," https://velodynelidar.com/wp-content/uploads/2019/12/63-9243-Rev-E-VLP-16-User-Manual.pdf.
[52] HESAI, "Mid-range mechanical lidar," https://www.hesaitech.com/product/xt32/.
[53] T. Huang, J. Liu, X. Zhou *et al.*, "V2x cooperative perception for autonomous driving: Recent advances and challenges," *arXiv preprint arXiv:2310.03525*, 2023.